

Colloidal CdSe Nanoplatelets, A Model for Surface Chemistry/Optoelectronic Property Relations in Semiconductor Nanocrystals

Shalini Singh,^{*,†,‡,§} Renu Tomar,^{†,‡} Stephanie ten Brinck,[§] Jonathan De Roo,^{†,‡,⊥} Pieter Geiregat,^{†,‡,§} José C. Martins,^{||} Ivan Infante,[§] and Zeger Hens^{†,‡,§}

[†]Physics and Chemistry of Nanostructures, Ghent University, 9000 Ghent, Belgium

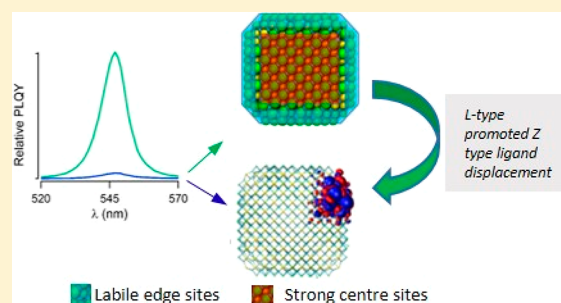
[‡]Center for Nano and Biophotonics, Ghent University, 9000 Ghent, Belgium

[§]Department of Theoretical Chemistry, Vrije Universiteit, 1081 HV Amsterdam, Netherlands

^{||}NMR and Structural Analysis Unit, Ghent University, 9000 Ghent, Belgium

Supporting Information

ABSTRACT: While the surface termination of quasi-spherical metal chalcogenide nanocrystals or quantum dots has been widely investigated, it remains unclear whether the ensuing surface chemistry models apply to similar nanocrystals with anisotropic shapes. In this work, we report on the surface-chemistry of 2D CdSe nanoplatelets, where we make use of an improved synthesis strategy that yields stable and aggregation free nanoplatelet suspensions with a photoluminescence quantum yield as high as 55%. We confirm that such nanoplatelets are enriched in Cd and, by means of ¹H nuclear magnetic resonance spectroscopy, we show that the Cd-rich surface is terminated by X-type carboxylate ligands. Not unlike CdSe quantum dots (QDs), entire cadmium carboxylate entities can be displaced by the addition of amines, and the desorption isotherm points toward a considerable binding site heterogeneity. Moreover, we find that even the slightest displacement of cadmium carboxylate ligands quenches the nanoplatelet photoluminescence. These experimental findings are further confirmed by density functional theory (DFT) calculations on a 5 monolayer model CdSe nanoplatelet. These simulations show that the most labile ligands are located in the vicinity of facet edges, and that the displacement of ligands from such edge sites creates midgap states that can account for the observed photoluminescence quenching. Next to extending surface chemistry insights from colloidal QDs to nanoplatelets, this work indicates that CdSe nanoplatelets constitute a unique nanocrystal model system to establish a comprehensive description of midgap trap states, which includes their structural, chemical, and electronic properties.



INTRODUCTION

The binding of ligands to the surface of colloidal semiconductor nanocrystals has attracted significant research interest because ligands are essential to optimize, tune, and tailor the physical and chemical properties of these functional nanomaterials.^{1–3} The multitude of possible surface chemistries was recently classified based on the nature of the ligand-nanocrystal bond.⁴ Here, the starting point was the covalent bond classification, which denotes ligands as L, X, or Z depending on the number of electrons the neutral ligand provides to the ligand-nanocrystal bond.⁵ Most importantly, this classification led to a better understanding of nanocrystal-ligand binding, postsynthesis ligand exchange reactions, and the interplay between the composition of the core nanocrystal and the ligand capping.^{4,6–9} Moreover, the same approach was applied later to describe the surface termination of metal oxide nanocrystals.¹⁰

For the case of colloidal metal chalcogenide nanocrystals or quantum dots (QDs), a comprehensive picture has emerged over the past 10 years on the relation between surface passivation and photoluminescence quantum yield

(PLQY).^{4,11} It was shown that the surface of divalent metal chalcogenides such as CdSe or PbS is metal-rich and passivated by 2 equiv of monovalent X-type ligands, such as carboxylates, phosphonates, or hydroxides.³ In the case of CdSe QDs, it was demonstrated that displacing such MX₂ salts from the CdSe surface results in a marked drop of the PLQY, which could be reversed by the readsorption of these Z-type ligands. More recently, DFT studies indicated that the loss of PLQY upon MX₂ displacement is linked to the formation of under-coordinated surface Se.¹¹ In particular, the formation of 2-coordinated Se results in localized states that can behave as traps for electrons or holes, depending on the Fermi level position. This model seems generally applicable to II–VI QDs.¹² In the case of CdTe QDs, charge carrier trapping was linked to the presence of 2-coordinated Te,¹³ whereas similarly 2-coordinated Te were shown to create optically active localized states that make possible nearly thresholdless optical amplification in HgTe QDs.¹⁴

Received: July 17, 2018

Published: September 26, 2018

Research that relates insight in surface chemistry to optoelectronic properties has been mainly focused on QDs. If anything, it is tacitly assumed that the concepts used to describe this relation for QDs apply equally to one-dimensional nanorods, two-dimensional nanoplatelets and other nanoscale objects.¹⁵ However, QDs are nanometer-size crystallites that have strongly curved surfaces composed of crystal facets that often measure a few square nanometers only. Hence, a sizable fraction of surface atoms will occupy sites at facet edges or vertices. This differs markedly from colloidal 2-D nanocrystals. CdSe nanoplatelets, for example, can be synthesized as structures that are just a few monolayers thick, but with atomically flat top and bottom surfaces that can measure several hundreds of square nanometer.^{16–18} Several authors have reported on a pronounced interplay between the ligand capping of nanoplatelets and their optical properties. For example, the absorption spectra of CdSe nanoplatelets were shown to be highly sensitive to changes in surface ligation.^{15,19} In addition, in spite of the large surface area, nanoplatelets can have a PLQY of up to 40%, even without overgrowth with a large band gap shell.^{20–24} However, research on CdSe nanoplatelets is often hampered by the limited colloidal stability of nanoplatelet dispersions and the unwanted stacking of nanoplatelets in multiplatelet bundles,^{25,26} two aspects that may be linked to the specific way ligands bind and pack to the nanoplatelet surface. This combination of highly promising properties and cumbersome processing calls for an in-depth study of the nanoplatelet surface chemistry. Here, the question stands out as to whether the concepts developed for highly curved, multifaceted 0D QDs can be transferred to nanoplatelets, which are terminated solely by atomically flat (100) interfaces.

In this study, we present a combined experimental and theoretical analysis of the surface chemistry of 2D nanoplatelets. First, we modified the classical synthesis protocol for 2-D CdSe nanoplatelets to achieve 5 monolayer (ML) nanoplatelets with ~55% quantum yield that form stable, aggregation free nanocolloids. Using nuclear magnetic resonance (NMR) spectroscopy, we demonstrate that these nanoplatelets are stabilized by tightly bound cadmium carboxylates. We further analyzed the distribution of binding sites on the surface by displacing these Z-type cadmium carboxylates through the addition of L-type ligands. The displacement isotherm points toward binding site heterogeneity on the nanoplatelet surface,²⁷ where at least two types of binding sites are required to model the displacement equilibrium, not unlike CdSe QDs.²⁷ This finding concurs with DFT calculations on a 5 ML model nanoplatelet, which enables us to localize the weaker binding sites at the platelet edges and the stronger sites on the facets. In addition, we show that the PL efficiency of nanoplatelets is highly sensitive to the displacement of Z-type ligands, where the removal of a very small fraction of Z-type ligands from edge sites indeed leads to the appearance of localized states in the band gap and quenching of PLQY. We thus conclude that in the case of CdSe nanoplatelets, the combination of a well-defined morphology, judicious ligand displacement experiments, and DFT simulations, yields in a complete picture of the surface termination that combines structural, chemical, and electronic insights. As such, this work constitutes a next step toward an atomistic understanding of colloidal semiconductor nanocrystals.

EXPERIMENTAL SECTION

Materials. Cadmium nitrate tetrahydrate $\text{Cd}(\text{NO}_3)_2 \cdot 4\text{H}_2\text{O}$, cadmium acetate tetrahydrate $\text{Cd}(\text{Ac})_2 \cdot 4\text{H}_2\text{O}$, CdO (>99.99) were purchased from Sigma-Aldrich. Myristic acid, sodium hydroxide NaOH, 1-octadecene (ODE, $\geq 90\%$) selenium powder (Se, -200 mesh, 99.999%) and oleic acid (OA, 90%) were purchased from Alfa Aesar. Hexane, methanol, and ethanol were purchased from Fiers. Cyclohexane- d_{12} (99.5% deuterated) was purchased from Euriso-top.

Synthesis of Cadmium Carboxylates. Cadmium myristate was prepared as previously reported.¹⁶ For the synthesis of cadmium oleate, CdO (0.642 g, 5 mmol) was mixed with 4.73 mL of OA and 5 mL of ODE in a three neck round-bottom flask. The mixture was degassed at 110 °C for 1 h, after which it was heated to 250 °C under nitrogen. When the mixture turned colorless, the heating mantle was removed, and the mixture was transferred to a vial for further use.

Synthesis of CdSe Nanoplatelets. In a typical synthesis, cadmium myristate (0.340 g, 0.6 mmol) and 25 mL of ODE were introduced in a three-neck flask and degassed under vacuum at room temperature. The solution was then heated to 250 °C under an inert atmosphere. At 250 °C, 0.024 g (0.3 mmol) of Se dispersed in 1 mL of ODE were swiftly injected into the solution. A minute later, 0.240 g of $\text{Cd}(\text{Ac})_2$ (0.9 mmol) was introduced. The reaction was allowed to proceed for 6 min at 250 °C, after which 1.5–2 mL of Cd-oleate, preheated at 100 °C, was injected. To stop the reaction, the heating mantle was removed immediately after this second injection, and the solution was allowed to cool down to 50 °C. The nanoplatelets were washed thoroughly by the purification techniques as described in detail in the Supporting Information (SI) Section S1. The nanoplatelets were then dispersed in hexane for further use.

Electron Microscopy. Bright field transmission electron microscopy (TEM) images and selected area electron diffraction (SAED) measurements were made using a Cs-corrected JEOL 2200FS TEM.

X-ray Diffraction. X-ray diffraction (XRD) has been used to analyze the crystal structure of the CdSe nanoplatelets. Diffractograms were recorded using a Thermo scientific ARL X'TRA model.

Dynamic Light Scattering. For dynamic light scattering (DLS) experiments, a Malvern Nano ZS was used in backscattering mode (173°). The samples were suspended in *n*-hexane, and measurements were done at 25 °C.

Optoelectronic Characterization. Absorption spectra were taken with a PerkinElmer Lambda 950 spectrometer. The nanoplatelet concentration was obtained using the intrinsic absorption coefficient $\mu_{p300} = 5.24 \times 10^5 \text{ cm}^{-1}$ for 5 ML CdSe nanoplatelets at 300 nm.²⁸ Photoluminescence measurements were done on an Edinburgh Instruments FLSP920 UV-vis-NIR spectrofluorometer using a 450 W xenon lamp as the excitation source. An excitation wavelength of 365 nm was used for all steady-state emission spectra. The photoluminescence quantum yield was measured using an integrating sphere.²⁹

Rutherford Backscattering Spectrometry. The stoichiometry of the CdSe nanoplatelets was determined by Rutherford backscattering spectrometry (RBS) using a 1.523 MeV 4He^+ beam at a tilt angle of 11°, with the detector positioned at a scattering angle of 170°. The atomic ratio between CdSe in the film was calculated from the integrated backscattering intensity on Cd and Se via the formula:

$$\frac{N_{\text{Cd}}}{N_{\text{Se}}} = \frac{I_{\text{Cd}}}{I_{\text{Se}}} \times \frac{Z_{\text{Se}}^2}{Z_{\text{Cd}}^2}$$

Nuclear Magnetic Resonance Spectroscopy. Samples for NMR spectroscopy were prepared by drying the purified QDs dispersion with a nitrogen flow and redispersing the nanoplatelets in 500 μL deuterated cyclohexane. The details on purification of nanoplatelets to make an NMR grade sample are given in SI Section S1. The sample temperature was set to 298.15 K. NMR measurements were recorded on a Bruker Avance III spectrometer operating at a ^1H frequency of 500.13 MHz and equipped with a BBI-Z probe or on a Bruker Avance II spectrometer operating at a ^1H frequency of 500.13 MHz and equipped with a TXO-Z probe. Quantitative ^1H spectra were recorded with a 20 s delay between scans to allow full relaxation

of all NMR signals. The quantification of the spectra was done by using the Digital ERETIC method.^{30,31} Diffusion measurements (2D diffusion ordered spectroscopy, DOSY) were performed using a double-stimulated echo sequence for convection compensation and with bipolar gradient pulses. Smoothed rectangle gradient pulse shapes were used throughout. The gradient strength was varied linearly from 2% to 98% of the probe's maximum value in 64 steps, with the gradient pulse duration and diffusion delay optimized to ensure a final attenuation of the signal in the final increment of less than 15% relative to the first increment. The NMR spectra are processed in IGOR Pro, version 6.32. To illustrate the diffusion resonances from all the protons of bound ligand clearly in the 2-D DOSY spectrum, 3 contour plots of different ¹H shift range were merged together as follows. The ¹H shift range for these contour plots are (1) -0.5–1.8 ppm, (2) 1.8–4 ppm, and (3) 4–7 ppm. The contours were intensified by two-fold in (2) and (3). Two-dimensional ¹H–¹H NOESY (nuclear Overhauser effect spectroscopy) spectra were acquired using a standard pulse sequence from the Bruker library, noesygpphpp. The NOESY mixing time was set to 300 ms with 4096 data points set in the direct dimension and 512 data points set in the indirect dimension. For 2D processing, before Fourier transformation, the 2D spectra were multiplied with a squared cosine bell function in both dimensions.

Density Functional Theory Calculations. For the DFT calculations, we constructed a nanoplatelet model of a 5 monolayer CdSe nanoplatelet by cutting a $3.07 \times 3.07 \times 1.25 \text{ nm}^3$ nonstoichiometric nanocrystal out of a bulk CdSe crystal. This model contains 295 Se atoms and 392 Cd atoms. To preserve charge neutrality, 194 chloride atoms were added to passivate the nanocrystal surface, leading to a final chemical composition of $[\text{CdSe}]_{295}(\text{CdCl}_2)_{97}$. The nanoplatelet model exposes six (100) facets, terminated at the vertices with either Cd-rich or Se-rich (111) facets. These structures have been optimized in the gas phase using the PBE exchange correlation functional³² and a double- ζ basis-set augmented with polarization functions.³³ All calculations were carried out with the CP2k software package.³⁴ Further details on the models employed are given in the text.

RESULTS AND DISCUSSION

We synthesized 5 ML CdSe platelets by the sequential injection of elemental Se dispersed in 1-octadecene and cadmium acetate in a hot reaction mixture containing cadmium myristate, following the method originally proposed by Ithurria et al.¹⁷ However, we arrested the reaction by injecting preheated cadmium oleate $[\text{Cd}(\text{OA})_2]$ instead of oleic acid and cooling down the entire reaction mixture. This adaptation was inspired by the idea that excess oleic acid can only exchange with ligands already bound to the CdSe surface—thus preserving the ligand surface concentration—whereas $\text{Cd}(\text{OA})_2$ is a Z-type ligand that can bind to CdSe surfaces and raise the ligand surface concentration. We found that using cadmium oleate instead of oleic acid as a reaction quencher resulted in nanoplatelet dispersions with a markedly improved colloidal stability. No platelet precipitation was observed over a time period of six months, and absorbance spectra were free of any background scattering. Both findings suggest that stopping the nanoplatelet synthesis by injection of $\text{Cd}(\text{OA})_2$ is an effective way to prevent the gradual formation of nanoplatelet stacks and bundles, which give rise to light scattering and drive nanoplatelet precipitation over time. Possibly, this is due to the formation of a more densely packed $\text{Cd}(\text{OA})_2$ ligand shell.

Figure 1a shows a low resolution bright field transmission electron microscopy (TEM) image of CdSe nanoplatelets synthesized according to the adapted protocol. Similar dark field images are shown in SI Section S2. Nanoplatelets lying

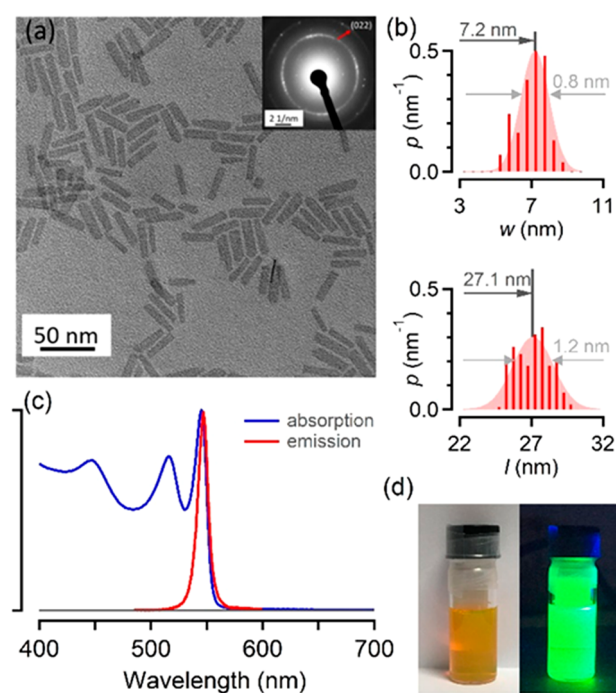


Figure 1. (a) Bright field TEM image of CdSe nanoplatelets with SAED pattern in the inset; (b) size histogram of the lateral dimensions of a batch of nanoplatelets as obtained from a set of TEM overview images; (c) absorbance and emission spectra of the CdSe nanoplatelets; and (d) photographs of a vial containing CdSe nanoplatelets in natural light and UV light.

mostly face-down on the TEM grid can be readily identified. The selected area electron diffraction (SAED) pattern (inset, Figure 1a) contains rings that can be indexed by means of the CdSe zinc-blende crystal structure. This assignment is confirmed by the X-ray diffractogram, which shows diffraction peaks at the angles expected for zinc blende CdSe (SI Section S2). Analyzing 200 nanoplatelets in such TEM images, we find that, for the example shown, top surfaces measure on average $27.1 \times 7.2 \text{ nm}^2$, with standard deviations of 1.2 and 0.8 nm on width and length, respectively (see Figure 1b, c). Other batches used in this study contain nanoplatelets with comparable dimensions, see SI Section S2.

The absorbance and emission spectra of CdSe nanoplatelet dispersions as shown in Figure 1c are characteristic of 5 monolayer platelets. In line with literature reports, the absorbance spectra feature two well-resolved transitions that correspond to the heavy-hole exciton at 545 nm and the light-hole exciton at 516 nm.^{16,35} The emission spectrum of these nanoplatelets consists of a single narrow band centered at 547 nm, with a full-width at half-maximum (fwhm) of 11.5 nm. Note that the Stokes shift between the heavy-hole exciton absorbance and emission line amounts to 2 nm at the most. After the first purification using ethanol/cyclohexane as the nonsolvent/solvent combination, a PLQY exceeding 50% is typically obtained, which compares favorably with the best literature reports on core-only CdSe nanoplatelets (<40%).^{20–22} By any means, these efficiencies are surprisingly high as compared to core CdSe QDs. Whereas these tend to have similar surface to volume ratios as few ML platelets, PLQYs typically attain a mere 5–10% at best. This difference suggests that CdSe nanoplatelets may have a nearly complete passivation of the (100) outer surfaces, or are better at

avoiding under-coordinated surface selenium, or other surface defects, from forming when the surface termination is incomplete.

To study the surface passivation of as-synthesized CdSe nanoplatelets, we first analyzed their composition using Rutherford Backscattering Spectrometry (RBS). Figure 2a

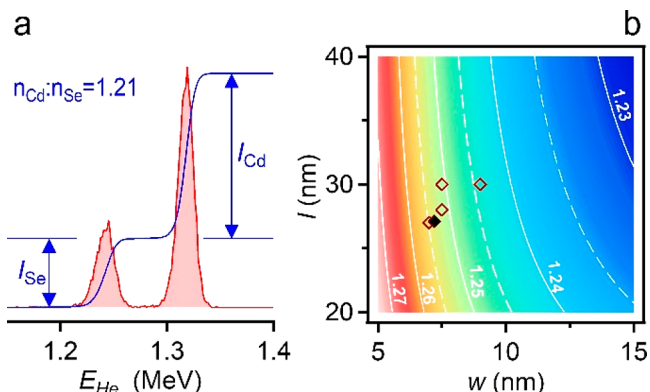


Figure 2. (a) Rutherford backscattering spectrum recorded on a thin film of 5 ML CdSe nanoplatelets spun on a Si substrate. The two signals correspond to backscattering from Se and Cd. The Z^2 weighted ratio of the backscattering intensities yields a Cd:Se ratio of 1.21. (b) Estimated Cd:Se ratio for 5 ML platelets as a function of the platelet width and length. The markers indicate the samples studied in this manuscript, where the filled marker represents the RBS sample.

shows an RBS spectrum of CdSe nanoplatelets that underwent up to 6 purification cycles using hexane and ethanol as the solvent and antisolvent. We implemented such a thorough purification scheme to obtain clean dispersions that are free of unbound ligands. The RBS spectrum features two pronounced signals that correspond to backscattering from Se and Cd on top of a near-zero background signal. From the intensity of both backscattering signals, we obtain a Cd:Se ratio of 1.21 ± 0.02 , a number that is somewhat smaller than the 1.255 ratio we would expect if the top and side nanoplatelet (100) surfaces

had a full excess Cd coverage (see Figure 2b). In addition, we found that the PLQY dropped after each purification cycle, to reach about 10% after six cycles, see SI Section S1. This PLQY drop is probably linked to the lower-than-expected Cd excess. At least in the case of CdSe QDs, it is known that the removal of Cd-carboxylate ligands induces surface traps that quench the photoluminescence.^{4,12} However, it is surprising to find the PLQY still at 10%—a value typical for as-synthesized CdSe QDs—after such extensive purification.

Figure 3a displays a representative ^1H NMR spectrum of a dispersion of 5 ML CdSe nanoplatelets in cyclohexane- d_{12} . Apart from the single narrow resonance \dagger at 1.38 ppm of cyclohexane, the spectrum only features the broadened resonances characteristic of bound ligands. The sole occurrence of broadened resonances suggests that the dispersion is well purified and only contains bound ligands and solvent. All resonances were assigned to protons from the oleyl chain as indicated in the inset of Figure 3a; an assignment that agrees with literature studies on oleate capped CdSe QDs. The characteristic resonance 5 of the alkene protons appears at 5.35 ppm and the methylene protons adjacent to the double bond at 2.055 ppm; the bulk of the methylene protons yields the intense resonance 3 at 1.320 ppm, and the resonance 6 of the methyl protons is retrieved at 0.912 ppm. A striking feature of the 1D ^1H NMR spectrum of the CdSe nanoplatelets is the line shape of the resonances, which consist of a relatively narrow center part atop an excessively broadened pedestal. This broad basis is notable in the region of the aliphatic protons, where the upfield side of the resonance extends well beyond the CH_3 resonance 6, and around the alkene proton resonance 5, whose downfield side only reaches the baseline at ~ 7.5 ppm. Such broad pedestals are absent in the case of 1D ^1H NMR spectra of oleate-capped CdSe QDs.³⁶ Possibly, this enhanced broadening reflects the reduced solvation of densely packed ligands on the flat (100) surfaces of the nanoplatelets.

Regardless of the interpretation, the particular line-shape of the oleyl proton resonances complicates the determination of the ligand surface concentration from integrated resonance intensities. Table 1 lists the surface concentration as estimated

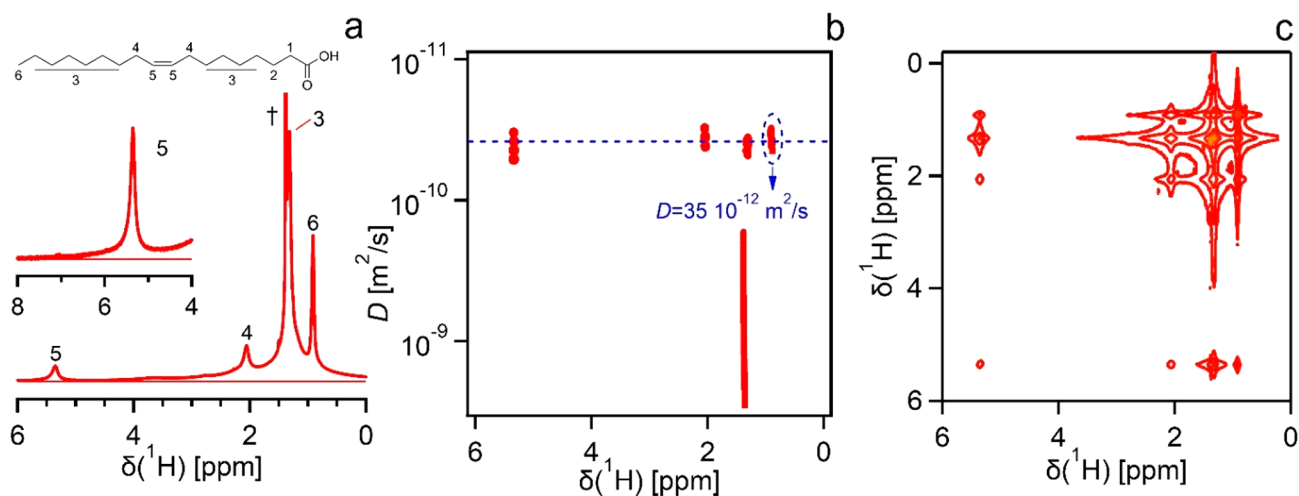


Figure 3. (a) 1D ^1H NMR spectrum of 5 ML CdSe nanoplatelets in cyclohexane- d_{12} . Inset: Zoom on the resonance of the alkene protons at ~ 5.35 ppm and the chemical structure of oleic acid, indicating the proton labeling used for assigning the resonances. (b) DOSY spectrum of 5 ML CdSe nanoplatelets in cyclohexane- d_{12} . The dashed line indicates the diffusion coefficient as obtained from fitting the decay of the intensity of the methyl protons x to a monoexponential decay (see SI Section S4); and (c) 2D NOESY spectrum of 5 ML CdSe nanoplatelets, featuring the intense, negative NOE cross peaks that are characteristic of bound oleate.

Table 1. Comparison of Integrated Peak Intensities and Ligand Surface Concentration Calculated from Methyl Proton and Alkene Proton Resonances along with the Estimated Cd:Se Ratio for the Given Dimensions of the Samples

sample	I_6/I_5	σ_{methyl} (nm ⁻²)	σ_{alkene} (nm ⁻²)	Cd:Se*
1	1.96	4.74	3.75	1.255
2	2.28	5.54	4.16	1.245
3	2.18	5.47	3.64	1.250
4	2.54	5.25	4.26	1.250
5	1.97	5.57	4.30	1.250

for 5 different samples using the integrated intensity I_6 and I_5 of the methyl and the alkene resonance, respectively. To obtain these numbers, we used a baseline correction as outlined in SI Section S3. As can be seen in Table 1, we found that the ratio I_6/I_5 showed a pronounced sample to sample variation, ranging from 1.97 to 2.54, while always exceeding the value of 1.5 that would be expected for oleyl chains. As we will discuss later, addition of butylamine to a nanoplatelet dispersion results in a partial displacement of Cd(OA)₂ from the nanoplatelet surface. As shown in SI Section S3, this leads to a progressive drop of the ratio I_6/I_5 from a value of 2.36 down to 1.66 for the example shown. This trend suggests that part of the signal intensity contained in the broad pedestal of the bound alkene resonance is lost in the background noise. In addition, any remaining cadmium myristate on the nanoplatelet surface will also contribute to the methyl resonance 6, and not to the alkene resonance 5, and thus increase the intensity ratio I_6/I_5 . In either case, the implication is that the methyl resonance 6 will yield the more reliable estimate of the ligand surface concentration.

On average, integration of the methyl resonance 6 yields a ligand surface concentration of 5.3 nm⁻² (see SI Section S3 for details on surface concentration calculations). A ligand surface concentration of 5.3 nm⁻² closely matches the surface concentration of 5.4 nm⁻² of Cd²⁺ cations at the CdSe (100) surface, indicating that the single excess monolayer of Cd²⁺ is charge compensated by two layers of carboxylates. However, such a surface concentration is significantly larger than the 4 nm⁻² one expects at best based on the molecular

volume of a single oleic acid molecule in liquid oleic acid. However, several studies have shown that due to the strong surface curvature, nanocrystal surfaces can accommodate more ligands than the corresponding macroscopic flat surface. In the case of gold for example, nanocrystals are expected to accommodate up to 6 dodecanethiol ligands/nm², 30% more than the corresponding self-assembled monolayer of thiols on flat gold surfaces.³⁷ Experimental studies effectively found surface concentrations of 5.3 nm⁻² for the 16-mercaptohexadecanoic acid/gold system,³⁸ and comparable numbers have been reported for other systems.³⁹ Similarly, molecular dynamics simulations showed that CdSe NCs pack 4.8 oleate ligands per nm² on their (100) facets, even if the oleate ligands are allowed to bind to sparsely occupied (111) facets.⁴⁰

We further analyzed to binding of carboxylate ligands to CdSe nanoplatelets using 2D DOSY and NOESY. As can be seen in Figure 3b, a DOSY spectrum recorded on the same dispersion of CdSe nanoplatelets in cyclohexane indicates that the bound ligand resonances come with a single diffusion coefficient that is about 50 times smaller than the self-diffusion of cyclohexane. As shown in SI Section S4, the bound ligand resonance intensities exhibit a monoexponential decay as a function of the square of the applied field gradient strength, from which a diffusion coefficient of 34.8 μm²/s is calculated. This value is about 12 times smaller than the diffusion coefficient of free oleic acid (see SI Section S4) in the absence of nanoplatelets ($D = 411 \mu\text{m}^2/\text{s}$). Moreover, it compares well to the diffusion coefficient that can be calculated for a randomly oriented diffusing sheet with the given dimensions of the CdSe nanoplatelets (see SI Section S4).⁴¹

In a separate set of experiments, we employed dynamic light scattering (DLS) as a simpler alternative technique to measure translational diffusion coefficient of the nanoplatelets (see SI Section S4). The diffusion coefficient values extracted from single-exponential decay of the correlation function of the scattered light intensity compares very well again with the calculated diffusion coefficient of unstacked randomly oriented nanoplatelet of the same dimension passivated by a monolayer of oleate ligands (described in SI Section S4). We thus conclude that similar to CdSe QDs, CdSe nanoplatelets can be seen as nonstoichiometric nanocrystals stabilized by tightly

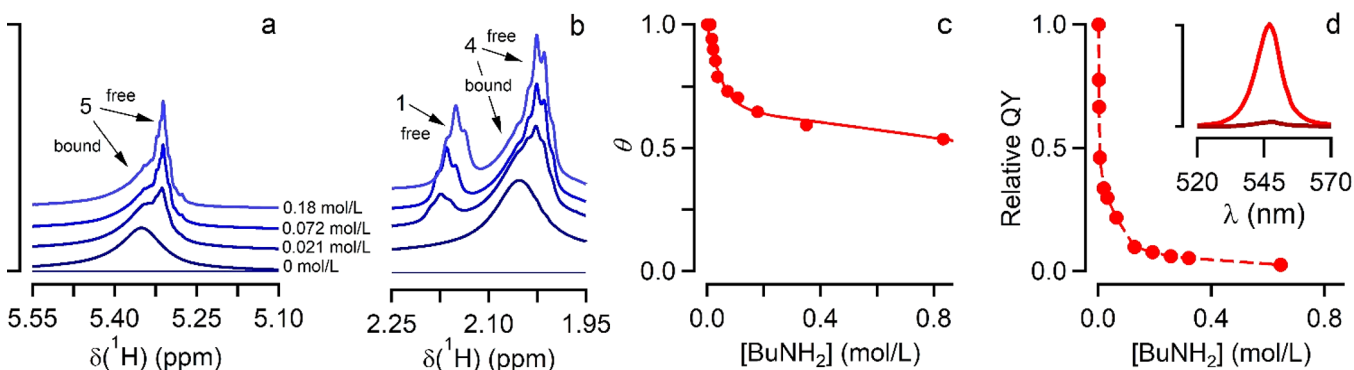
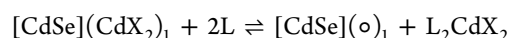


Figure 4. (a) Zoom on the alkene resonance 5 in the ¹H NMR spectra of a CdSe nanoplatelet dispersion (nanoplatelet concentration: 11.7 μM, bound carboxylate concentration of 33.7 mM) to which BuNH₂ has been added with concentrations as indicated. The resonances assigned to bound and free cadmium oleate have been indicated. (b) The same, but zooming in on the resonances 1 (α-CH₂) and 4 of the oleyl chain. (c) Fractional surface coverage of oleate at the surface of CdSe nanoplatelets, calculated relative to the initial surface concentration, as a function of the BuNH₂ concentration in solution. The full line represents a fit to a two-site adsorption model. (d) Photoluminescence quantum yield (PLQY) as a function of the BuNH₂ concentration. Inset: photoluminescence spectrum at (bright red) the start and (dark red) the end of the titration. The dashed line is a guide to the eye.

bound carboxylate ligands (X) or, equivalently, as stoichiometric nanostructures stabilized by tightly bound cadmium carboxylates (CdX_2).^{6,34} As can be seen in Figure 3c, all resonances assigned to bound carboxylate protons feature strongly negative NOE cross-peaks. Hence, also in the case of nanoplatelets, so-called negative NOE's can be seen as a sensitive indicator for ligand-nanocrystal interactions.

In the case of CdSe QDs, it is known that the photoluminescence efficiency is linked to the surface coverage by cadmium carboxylates.^{4,42–44} Moreover, such CdX_2 ligands can be displaced by L-type ligands such as alkylamines, which is an equilibrium reaction that enables the ligand surface concentration to be finely adjusted.²⁷ Here, we used the NMR spectra recorded before and after addition of butylamine (BuNH_2) to a dispersion of CdSe nanoplatelets in cyclohexane to analyze the occurrence of amine-induced CdX_2 displacement, BuNH_2 being an L-type ligand with a high displacement potency.⁴² Importantly, addition of BuNH_2 did not affect the nanoplatelet morphology, nor did it result in shifts of the excitonic features in the absorption spectra (see SI Section S5). BuNH_2 addition did, however, lead to significant changes in the NMR spectrum. Focusing on the resonances 4 and 5, it can be seen that a second, narrow resonance develops at the upfield side of the original, broad resonances (see Figure 4a, b) during a BuNH_2 titration. These additional resonances gain intensity as the concentration of BuNH_2 is increased, at the expense of the intensity of the broad resonances. Similar changes occurred with CdSe QDs, in which case the occurrence of two resonances was assigned to the presence of bound and displaced CdX_2 exhibiting a slow displacement equilibrium.²⁷ Interestingly, while the $\alpha\text{-CH}_2$ resonance 1 of bound CdX_2 cannot be resolved due to excessive line broadening, displaced CdX_2 exhibits a well resolved $\alpha\text{-CH}_2$ resonance 1, which appears as a triplet at around 2.15 ppm. Importantly, the NOESY spectrum of the CdSe sample after the displacement experiment features negative NOE cross-peaks for oleate chain protons and amine protons (see SI Section S5). This indicates that displaced CdX_2 still interact with the platelet surface, most likely since displacement results in a dynamic equilibrium between dissolved CdX_2 coordinated by BuNH_2 and surface-bound CdX_2 , similar to what was demonstrated for CdSe QDs. We thus infer that the two sets of oleate resonances reflect two pools of CdX_2 —free and bound—that exhibit a slow chemical exchange.

We used the intensity of the $\alpha\text{-CH}_2$ resonance 1 of displaced CdX_2 to quantify the fraction of the originally surface bound cadmium carboxylate at each step in a BuNH_2 titration of a CdSe nanoplatelet dispersion. This enabled us to determine a displacement isotherm, which represents the CdX_2 surface coverage as a function of the BuNH_2 concentration. As can be seen in Figure 4c, this isotherm exhibits a pronounced drop in surface coverage at low BuNH_2 concentrations, in combination with a persistent surface coverage of 50–60% up to BuNH_2 concentrations of 0.8 mol/L. We analyze this isotherm with the two-site model introduced by Drijvers et al. to account for binding site heterogeneity in the case of quasi-spherical CdSe nanocrystals.²⁷ This model assumes a coupled equilibrium, where BuNH_2 can displace CdX_2 from two sets of binding sites, a first with a low and a second with a high binding energy:



Here, $[\text{CdSe}]$ represents the stoichiometric nanocrystal core, (CdX_2) a surface bound cadmium carboxylate, and (\circ) an empty surface site. Moreover, L stands for BuNH_2 , and we have explicitly introduced a 2-equiv displacement as found in the case of CdSe QDs.²⁷ Figure 4c represents a simulation of the displacement isotherm using this coupled, two-site displacement equilibrium. Similar to the case of CdSe QDs, this description captures the combination of a rapid reduction of surface coverage at low BuNH_2 with the persistence of bound CdX_2 at high BuNH_2 concentration. As compared to CdSe QDs, we find a similar equilibrium constant K_1 for displacement from the weaker binding sites in the case of CdSe nanoplatelets, yet the latter feature a notably smaller fraction of weak binding sites (see Table 2). In combination with the large

Table 2. Initial Surface Concentration σ of Carboxylate Ligands and Parameters Used to Simulate the BuNH_2 Displacement Isotherm Using a 2 Site Model for the Case of CdSe Nanoplatelets and CdSe QDs, Including (K_1 , K_2) the Equilibrium Constant for Displacement of Weakly and Strongly Bound CdX_2 and (α) the Fraction of Weakly Bound CdX_2 ^a

system	σ (nm^{-2})	α	K_1	K_2
platelets	5.4	0.375	3.0	0.002
QDs	3.2	0.525	3.0	0.01

^aData for CdSe QDs were taken from ref 27.

surface concentration of CdX_2 , this yields a surface concentration of strongly bound CdX_2 of $\approx 3.4 \text{ nm}^{-2}$ in the case of nanoplatelets, a number that is markedly larger than the $\sim 1.5 \text{ nm}^{-2}$ we obtain for CdSe QDs.

Figure 4d represents the evolution of the relative PLQY during the different steps of a BuNH_2 titration that was run in parallel to the determination of the displacement isotherm. Importantly, we observe a sharp drop of the photoluminescence efficiency even during the initial stages of the titration where only a minor fraction of surface ligands has been displaced. For example, using the simulation of the experimental isotherm, we estimate that the removal of a mere 1% of the surface ligands reduces the relative PLQY by 25% in the first step of the titration. Hence, opposite from CdSe QDs, there seems to be no threshold surface coverage above which the PLQY can be preserved.⁴ Moreover, this again indicates toward the large fraction of strongly binding oleates on the surface which prevents any change in the strain state of nanoplatelet crystal structure.^{15,44}

To better understand the passivation of the nanoplatelets by ligands and the concomitant electronic structure of nanoplatelets, we performed a density functional theory (DFT) analysis. As shown in Figure 5, we built a 5 ML model platelet with a $3.07 \times 3.07 \text{ nm}^2$ (100) top facet and a surface fully passivated with CdCl_2 . Using CdCl_2 instead of Cd oleate as a Z-type ligand limits the computational effort and avoids the additional degrees of freedom that come with the different possible binding modes of carboxylates to Cd surface sites. We focused first of all on the displacement of a single Z-type ligand by BuNH_2 according to the equilibrium (1) and calculated the displacement energy for different locations on the nanoplatelet

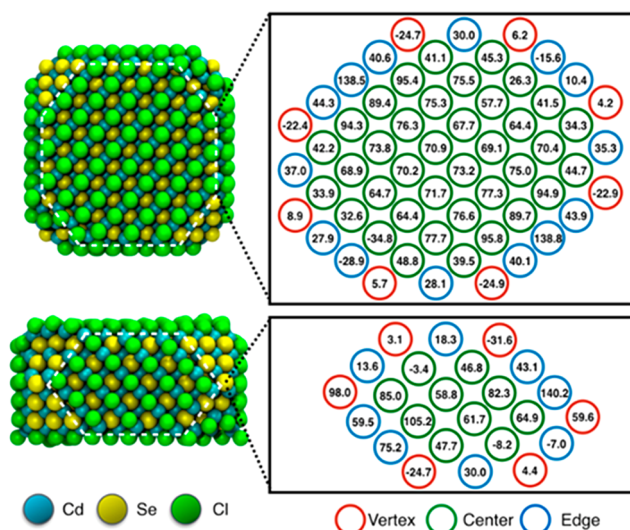


Figure 5. Exposed top and side facet of with the computed total displacement (desorption and coordination) energies in kJ/mol calculated for different binding sites.

surface. Figure 5 represents the thus-obtained displacement energies. The small size of the nanoplatelet top surface makes that most of the lattice positions remain relatively close to edges or vertices. Nevertheless, a qualitative trend shows up, where the most labile Z-type ligands are found at the edges and vertices of the platelet. More quantitatively, we found an average displacement energy of 18.1 kJ/mol for the binding sites within 2 atomic lines of a (100) edge, and 74.7 kJ/mol for the binding sites further away from these edges. Clearly, this result confirms that the picture of binding site heterogeneity put forward for CdSe QDs applies to CdSe nanoplatelets as well, and indicates that the weak bindings sites are mostly related to the nanoplatelet edges.

At this point, it is interesting to compare the simulation results with the experimental findings on ligand displacement of CdSe QDs and nanoplatelets. First, starting from the idea that weak binding sites are related to surface Cd within the first or the second atomic line from an edge, we estimate that a $7 \times 27 \text{ nm}^2$ 5 ML platelet will have 32.5% weak and 67.5% strong ligands (see SI Section S6). This number comes close to the estimated fraction $\alpha = 0.375$ of weak ligands we obtained from simulating the displacement isotherm (see Table 2); a point that supports the link between weak binding sites and nanocrystal edges. Second, the average displacement energy of the weakest half of the binding sites amounted to -3 kJ/mol in the case of CdSe QDs, whereas we obtain 18.1 kJ/mol in the case of CdSe nanoplatelets. While this merely reflects the smaller number of edge and vertex sites, it also implies that the correspondence of the displacement equilibrium constant between QDs and nanoplatelets may originate from the way the isotherm is measured. In both cases, we used purified dispersions. This could mean that ligands with a binding energy smaller than a certain threshold have been stripped, which would create an identical starting point for both titrations. In this respect, the larger fraction of strongly binding ligands in the case of CdSe nanoplatelets may explain why, even after 6 purification cycles, the ligand surface density exceeds 5 nm^{-2} .

Given the indications that BuNH₂ strips Cd oleate ligands from sites close to the platelet edges and concomitantly

quenches the photoluminescence efficiency, we analyzed in a second step the electronic structure of the model nanoplatelet at different ligand surface concentrations. Since the model nanoplatelet offers large and flat (100) top and side planes, many different patterns of successive ligand displacement are possible, which can all result into different outcomes. To minimize this effect, we displaced ligands only from the edge sites as these are the most labile according to the above analysis. We then followed a two-step displacement, where we reduced the surface concentration on the top (100) facet from $5.50 \text{ ligands/nm}^2$ first to 4.90 nm^{-2} and then to 4.20 nm^{-2} . At each removal, we performed a structural relaxation and checked for the presence of dicoordinated Se, as these types of surface atoms are the likely origin of midgap states.¹¹

In Figure 6, we show the electronic structures of the model nanoplatelet with a pristine surface composition (left, model

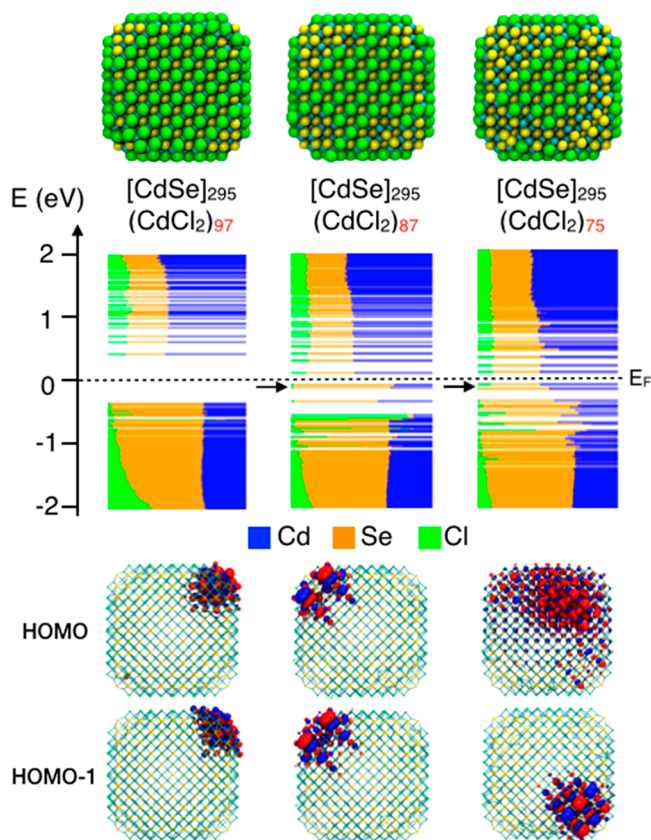


Figure 6. Atomistic and electronic structure of the model nanoplatelet for which (left) no, (center) 10 and (right) 22 CdCl₂ ligands were removed. The black arrows indicate the midgap states that form upon removal of CdCl₂ from the pristine nanoplatelet. At the bottom, contour plots of the highest occupied molecular orbitals of the three systems are shown.

1), followed by the nanoplatelet with 10 (center, model 2) and 22 (right, model 3) CdCl₂ ligands removed. Note that in the case of a $27 \times 7 \text{ nm}^2$ nanoplatelet, 10 and 22 ligands this would amount to about 0.25 and 0.5% of the ligand surface coverage, numbers that agree with the ligand displacement during the initial stage of the BuNH₂ titration. Each line in the figure represents one molecular orbital (MO), and the colored sections measure the contribution of different atom types to this MO. Each plot is centered around its Fermi level to allow for a more straightforward comparison between the different

models. One readily sees that model 1 features a band gap free of midgap states. At ~ 0.8 eV, this band gap is quite small and rather different from the experimental one. This is a known problem of density functional theory within the generalized gradient approximation, like the PBE employed here. Especially for CdSe, such an approach tends to largely underestimate the bandgap energy. At the same time, however, this method allows to tackle large systems, for which it provides accurate geometrical structures and energetics, and correct composition of the MOs in terms of the constituting atomic orbitals.¹²

Opposite from the pristine nanoplatelet model, 3 and 4 midgap states appear in the band gap when CdCl₂ ligands are removed from facet edges in model 2 and 3, respectively. This concurs with the respective formation of 3 and 4 dicoordinated Se atoms. To verify the relation between midgap states and dicoordinated surface Se, we analyzed the orbital composition of these midgap states (black arrows lines in Figure 6) and found that these states are localized on a single atom, or a small group of atoms, and closely resemble uncoupled p-orbitals on dicoordinated Se (Figure 6, orbitals belonging to model 2 and 3). Note that the frontier orbitals in the pristine nanoplatelet (Figure 6, orbitals belonging to model 1) shown in Figure 6 seem to present a facet specific localization on the (111) surfaces. Apparently, the larger dimension of the (100) surfaces against the smaller (111) leads to a reduced orbital mixing between the atoms lying on these facets. This was evident when we projected the density of states on the (100) and (111) facets (SI Section S7). Clearly, near the valence band edge, MOs are dominated by atomic orbitals lying on the (111) facets, while deeper in the valence band, the (100) related states emerge. Overall, despite this unusual feature, we do not regard any of the (111) states as traps or relevant for our purposes. At more realistic sizes than the model chosen for these calculations, the number of (111) MOs remains constant, as the size of this facet is unchanged, while the number of (100) MOs grows significantly with the size of the platelet. Overall, these calculations indicate that stripping Z-type ligands from the edges will readily generates midgap states that will reduce the efficiency of radiative recombination. Clearly, this conclusion agrees with our experimental findings where the initial ligand stripping—attributed to CdX₂ removal from edge or near-edge sites—concurr with an immediate loss of photoluminescence efficiency.

Understanding the structural and chemical aspects of ligand binding and elucidating the impact of ligand binding on electronic structure are long-standing goals in nanocrystal research. In this respect, CdSe nanoplatelets appear as a unique model system to study the properties of surface defects. Mostly due to the straightforward nanoplatelet morphology, weak binding of cadmium carboxylates can be ascribed almost exclusively to near-edge sites; a conclusion that is supported by the combined experimental/theoretical approach to nanocrystal surface chemistry implemented here. This localization of labile ligands leads to realistic predictions on the nature of the trap states created by ligand displacement. Importantly, these trap states have properties such as trapping times or characteristic defect emission, that can be tested in future experiments. We believe such studies can provide the atomically precise description of trap states needed to support the wide range of optical, magnetic, or charge transport properties of nanocrystals and nanocrystals assemblies assigned to trap states.

CONCLUSIONS

By means of an improved protocol to quench the formation of 5 monolayer CdSe nanoplatelets we obtain nanoplatelet dispersions with long-term colloidal stability and a high photoluminescence quantum yield. On the basis of such dispersions, we analyze the surface chemistry of CdSe nanoplatelets through a combination of elemental analysis and solution NMR spectroscopy. Similar to CdSe QDs, we find that CdSe nanoplatelets are Cd-rich crystallites, terminated by oleate ligands. Even if solution NMR resonances exhibit a pronounced line broadening, ligand surface concentrations could be estimated on average at 5.3 nm^{-2} . We show that addition of an L-type ligand such as BuNH₂ leads to cadmium carboxylate displacement, where even a reduction of the surface coverage by 1% impacts on the photoluminescence quantum yield. The displacement isotherm points toward a heterogeneous set of binding sites, which features a larger fraction of strong binding sites than CdSe QDs. This finding is corroborated by DFT calculations on a 5 monolayer model nanoplatelet, which predict significantly weaker binding at sites within 2 atomic lines from the nanoplatelet edges. Moreover, we find that displacement of ligands from these edge sites leads to the formation of mid gap states that can be linked to the creation of dicoordinated selenium. This localization of trap states at the platelet edges puts forward CdSe nanoplatelets as a nanocrystal model system for obtaining a comprehensive, atomistically precise description of midgap states.

ASSOCIATED CONTENT

Supporting Information

The Supporting Information is available free of charge on the ACS Publications website at DOI: 10.1021/jacs.8b07566.

Additional Experimental details, XRD spectrum, DLS measurements, NMR analyses, diffusion coefficient calculations, electronic structures of CdSe model nanoplatelets, and so forth (PDF)

AUTHOR INFORMATION

Corresponding Author

*Shalini.Singh@ugent.be

ORCID

Shalini Singh: 0000-0001-8607-8383

Jonathan De Roo: 0000-0002-1264-9312

Pieter Geiregat: 0000-0001-7217-8738

Ivan Infante: 0000-0003-3467-9376

Zeger Hens: 0000-0002-7041-3375

Present Address

¹J.D.R- Department of Chemistry, Columbia University, New York, New York 10027, United States.

Notes

The authors declare no competing financial interest.

ACKNOWLEDGMENTS

The authors acknowledge support by the European Commission via the Marie-Sklodowska Curie action Phonsi (H2020-MSCA-ITN-642656), the Belgian Science Policy Office (IAP 7.35, photonics@be) and BOF-UGent (GOA no. 01G01513). Sh.S. would like to acknowledge FWO postdoctoral funding (FWO17/PDO/184). I.I. would like to thank The Netherlands Organization of Scientific Research (NWO) for providing financial support within the Innovational Research Incentive

(Vidi) Scheme. DFT calculations were carried out on the Dutch national e-infrastructure with the support of SURF Cooperative.

REFERENCES

- (1) Talapin, D. V.; Lee, J.-S.; Kovalenko, M. V.; Shevchenko, E. V. *Chem. Rev.* **2010**, *110*, 389–458.
- (2) Kovalenko, M. V.; Manna, L.; Cabot, A.; Hens, Z.; Talapin, D. V.; Kagan, C. R.; Klimov, V. I.; Rogach, A. L.; Reiss, P.; Milliron, D. J.; Guyot-Sionnest, P.; Konstantatos, G.; Parak, W. J.; Hyeon, T.; Korgel, B. A.; Murray, C. B.; Heiss, W. *ACS Nano* **2015**, *9*, 1012–1057.
- (3) Hens, Z.; Martins, J. C. *Chem. Mater.* **2013**, *25*, 1211–1221.
- (4) Anderson, N. C.; Hendricks, M. P.; Choi, J. J.; Owen, J. S. *J. Am. Chem. Soc.* **2013**, *135*, 18536–18548.
- (5) Green, M. L. H.; Parkin, G. J. *J. Chem. Educ.* **2014**, *91*, 807–816.
- (6) Ji, X.; Copenhagen, D.; Sichmeller, C.; Peng, X. *J. Am. Chem. Soc.* **2008**, *130*, 5726–5735.
- (7) Hughes, B. K.; Ruddy, D. A.; Blackburn, J. L.; Smith, D. K.; Bergren, M. R.; Nozik, A. J.; Johnson, J. C.; Beard, M. C. *ACS Nano* **2012**, *6*, 5498–5506.
- (8) Bealing, C. R.; Baumgardner, W. J.; Choi, J. J.; Hanrath, T.; Hennig, R. G. *ACS Nano* **2012**, *6*, 2118–2127.
- (9) Saniepay, M.; Mi, C.; Liu, Z.; Abel, E. P.; Beaulac, R. *J. Am. Chem. Soc.* **2018**, *140*, 1725–1736.
- (10) De Roo, J.; Van den Broeck, F.; De Keukeleere, K.; Martins, J. C.; Van Driessche, I.; Hens, Z. *J. Am. Chem. Soc.* **2014**, *136*, 9650–9657.
- (11) Houtepen, A. J.; Hens, Z.; Owen, J. S.; Infante, I. *Chem. Mater.* **2017**, *29*, 752–761.
- (12) Giansante, C.; Infante, I. *J. Phys. Chem. Lett.* **2017**, *8*, 5209–5215.
- (13) Boehme, S. C.; Azpiroz, J. M.; Aulin, Y. V.; Grozema, F. C.; Vanmaekelbergh, D.; Siebbeles, L. D. A.; Infante, I.; Houtepen, A. J. *Nano Lett.* **2015**, *15*, 3056–3066.
- (14) Geiregat, P.; Houtepen, A. J.; Sagar, L. K.; Infante, I.; Zapata, F.; Grigel, V.; Allan, G.; Delerue, C.; Van Thourhout, D.; Hens, Z. *Nat. Mater.* **2017**, *17* (1), 7.
- (15) Zhou, Y.; Buhro, W. E. *J. Am. Chem. Soc.* **2017**, *139*, 12887–12890.
- (16) Ithurria, S.; Bousquet, G.; Dubertret, B. *J. Am. Chem. Soc.* **2011**, *133*, 3070–3077.
- (17) Ithurria, S.; Tessier, M. D.; Mahler, B.; Lobo, R. P. S. M.; Dubertret, B.; Efros, A. L. *Nat. Mater.* **2011**, *10*, 936–941.
- (18) Gerdes, F.; Navío, C.; Juárez, B. H.; Klinke, C. *Nano Lett.* **2017**, *17*, 4165–4171.
- (19) Zhou, Y.; Wang, F.; Buhro, W. E. *J. Am. Chem. Soc.* **2015**, *137*, 15198–15208.
- (20) Bouet, C.; Tessier, M. D.; Ithurria, S.; Mahler, B.; Nadal, B.; Dubertret, B. *Chem. Mater.* **2013**, *25* (8), 1262–1271.
- (21) Mahler, B.; Nadal, B.; Bouet, C.; Patriarche, G.; Dubertret, B. *J. Am. Chem. Soc.* **2012**, *134*, 18591–18598.
- (22) Polovitsyn, A.; Dang, Z.; Movilla, J. L.; Martín-García, B.; Khan, A. H.; Bertrand, G. H. V.; Brescia, R.; Moreels, I. *Chem. Mater.* **2017**, *29*, 5671–5680.
- (23) Tessier, M. D.; Javaux, C.; Maksimovic, I.; Lorette, V.; Dubertret, B. *ACS Nano* **2012**, *6* (8), 6751–6758.
- (24) She, C.; Fedin, I.; Dolzhnikov, D. S.; Dahlberg, P. D.; Engel, G. S.; Schaller, R. D.; Talapin, D. V. *ACS Nano* **2015**, *9*, 9475–9485.
- (25) Antanovich, A.; Prudnikau, A.; Matsukovich, A.; Achtstein, A.; Artemyev, M. *J. Phys. Chem. C* **2016**, *120*, 5764–5775.
- (26) Guzelturk, B.; Erdem, O.; Olutas, M.; Kelestemur, Y.; Demir, H. V. *ACS Nano* **2014**, *8*, 12524–12533.
- (27) Drijvers, E.; De Roo, J.; Martins, J. C.; Infante, I.; Hens, Z. *Chem. Mater.* **2018**, *30*, 1178.
- (28) Achtstein, A. W.; Antanovich, A.; Prudnikau, A.; Scott, R.; Woggon, U.; Artemyev, M. *J. Phys. Chem. C* **2015**, *119*, 20156–20161.
- (29) de Mello, J. C.; Wittmann, H. F.; Friend, R. H. *Adv. Mater.* **1997**, *9*, 230–232.
- (30) Akoka, S.; Barantin, L.; Trierweiler, M. *Anal. Chem.* **1999**, *71*, 2554–2557.
- (31) Silvestre, V.; Goupry, S.; Trierweiler, M.; Robins, R.; Akoka, S. *Anal. Chem.* **2001**, *73*, 1862–1868.
- (32) Perdew, J. P.; Burke, K.; Ernzerhof, M. *Phys. Rev. Lett.* **1997**, *78*, 1396–1396.
- (33) VandeVondele, J.; Hutter, J. *J. Chem. Phys.* **2007**, *127*, 114105.
- (34) Hutter, J.; Iannuzzi, M.; Schiffrmann, F.; VandeVondele, J. *Wiley Interdiscip. Rev. Comput. Mol. Sci.* **2014**, *4*, 15–25.
- (35) Gao, Y.; Weidman, M. C.; Tisdale, W. A. *Nano Lett.* **2017**, *17*, 3837–3843.
- (36) Fritzing, B.; Capek, R. K.; Lambert, K.; Martins, J. C.; Hens, Z. *J. Am. Chem. Soc.* **2010**, *132*, 10195–10201.
- (37) Djebaili, T.; Richardi, J.; Abel, S.; Marchi, M. *J. Phys. Chem. C* **2013**, *117*, 17791–17800.
- (38) Hinterwirth, H.; Kappel, S.; Waitz, T.; Prohaska, T.; Lindner, W.; Lämmerhofer, M. *ACS Nano* **2013**, *7*, 1129–1136.
- (39) Smith, A. M.; Johnston, K. A.; Crawford, S. E.; Marbella, L. E.; Millstone, J. E. *Analyst* **2017**, *142*, 11–29.
- (40) De Nolf, K.; Cosseddu, S. M.; Jasieniak, J. J.; Drijvers, E.; Martins, J. C.; Infante, I.; Hens, Z. *J. Am. Chem. Soc.* **2017**, *139*, 3456–3464.
- (41) Bagheri, G.; Bonadonna, C. *Powder Technol.* **2016**, *301*, 526–544.
- (42) Chen, P. E.; Anderson, N. C.; Norman, Z. M.; Owen, J. S. *J. Am. Chem. Soc.* **2017**, *139*, 3227–3236.
- (43) Campos, M. P.; Hendricks, M. P.; Beecher, A. N.; Walravens, W.; Swain, R. A.; Cleveland, G. T.; Hens, Z.; Sfeir, M. Y.; Owen, J. S. *J. Am. Chem. Soc.* **2017**, *139*, 2296–2305.
- (44) Yao, Y.; Zhou, Y.; Sanderson, W. M.; Loomis, R. A.; Buhro, W. E. *Chem. Mater.* **2018**, *30*, 2848–2857.